Chemical Geology 709 (2026) 123355

Contents lists available at ScienceDirect

Chemical Geology

journal homepage: www.elsevier.com/locate/chemgeo

Geochemical behavior of rare earth elements in pore fluids of turbidite sediments from South Taiwan

Yi Huang [a,b], Eric Douville [c], Christophe Colin [a,*], Zhifei Liu [d], Bin Li [b,e], Qiong Wu [f], Rosella Pinna-Jamme [a], Andrew Tien-shun Lin [g]

[a] Université Paris-Saclay, CNRS, GEOPS, 91405 Orsay, France
[b] Key Laboratory of Metallogenic Prediction of Nonferrous Metals and Geological Environment Monitoring (Ministry of Education), School of Geosciences and Info-physics, Central South University, 410083 Changsha, China
[c] Laboratoire des Sciences du Climat et de l'Environnement, LSCE/IPSL, CEA, CNRS-UVSQ, Université Paris-Saclay, F-91191 Gif-sur-Yvette, France
[d] State Key Laboratory of Marine Geology, Tongji University, Shanghai 200092, China
[e] School of New Energy and Mining, Xinjiang University of Technology, Hetian 848000, Xinjiang, China
[f] College of Oceanography, Hohai University, 210098 Nanjing, China
[g] Department of Earth Sciences, National Central University, Jhongli 32001, Taiwan

ARTICLE INFO

Editor: Christian France-Lanord

Keywords:
Pore fluids
Rare earth elements
Turbidites
Early diagenesis
South China Sea

ABSTRACT

Major and rare earth elements (REEs) concentrations in sediment pore fluids are crucial for tracking biogeochemical processes during early diagenesis. However, the low concentrations and volumes typically sampled, particularly from long sedimentary sequences, limit our understanding of the REE behaviors in pore fluids. Here, major and trace elements have been analyzed on pore fluids from nine cores collected along the Penghu and Gaoping submarine canyons (SE Taiwan), in order to constrain diagenesis processes in sediments characterized by turbidite deposits and to determine their potential influence on the REE behavior in pore fluids. The ΣREE decrease from 600 to 200 pM in the upper 500 cm, with the maximum value attributed to the dissolution of Mn oxides in the redox transition zone. A decrease with depth of Ca and Mg concentrations are most probably associated with the formation of authigenic carbonate during the sulfate reduction process. This process absorbs REE from pore fluids without the REE fractionations. At deeper depth, an HREE enriched pattern is observed in core along the Penghu Canyon and might be linked to the degradation of organic matter in the methanogenesis zone. For cores located along the Gaoping Canyon, super-chondritic Y/Ho ratios comparable to seawater suggest a pronounced mixing of pore fluids with seawater and stronger scavenging of detrital sediments in the turbidity system. Overall, our results indicate that the REE concentrations in the pore fluids are relatively low and partitioning at deep depth in South Taiwan, REE distributions of pore fluids from turbidites sequences show a non-steady state variations in the high energy depositional setting.

1. Introduction

Sediment diagenesis significantly influences biogeochemical cycling of elements, benthic fluxes to overlying waters, and the preservation of paleo-environmental signatures in sediments (e.g. Berner, 1980; Boudreau, 2000; Hesse and Schacht, 2011; Hood et al., 2018; Du et al., 2025). According to the electron acceptors sequentially utilized by microbial communities ($O_2 > NO_3^- > MnO_2 > Fe(OH)_3 > SO_4^{2-} > CH_2O$), sediment redox zones develop with increasing burial depth (e.g., Froelich et al., 1979; Arndt et al., 2013). Ideally, they can be divided into an oxidized (oxygen-rich) zone, a sub-oxidized (oxygen-poor) zone, an anoxic zone, a sulfide zone and a methanogenesis zone. Trace element behavior during these processes, particularly in highly reactive surface layers (<1–2 m), has been extensively studied and these studies primarily form the basis for our current understanding of fluid migration in subseafloor systems (e.g., Elderfield and Sholkovitz, 1987; Haley et al., 2004; Torres et al., 2004; Abbott et al., 2015; Deng et al., 2022; Steiner et al., 2023). However, datasets on trace element concentrations in long sediment sequences remain limited due to the low concentrations and volumes available as well as the challenges associated with the collection and analysis of pore fluids (Smrzka et al., 2019). This hinders our knowledge about the potential impact on the pore fluids of different

* Corresponding author.
E-mail address: christophe.colin@universite-paris-saclay.fr (C. Colin).

https://doi.org/10.1016/j.chemgeo.2026.123355
Received 29 August 2025; Received in revised form 22 February 2026; Accepted 4 March 2026
Available online 5 March 2026

processes during the early-diagenesis of sediments, particularly in the upper sediment sequences.

Moreover, the rare earth elements (REEs) in pore fluids are powerful tools for tracing biogeochemical processes and for reconstructing the environment in which sediment diagenesis takes place (e.g., Bau and Dulski, 1996; Frimmel, 2009; Kim et al., 2012; Zwicker et al., 2018). The fractionation of REEs in sediments and pore fluids is due to several factors such as REE provenance and sources, dissolution or co-precipitation effects, processes of absorption/desorption, physic-chemical parameters of the medium and redox state, and finally the stability in solutions favored or not by the presence of ligands and the process of complexation (Williams-Jones et al., 2012; Bayon et al., 2020; Li et al., 2022). A large dynamic range of REE fractionation and patterns can be found in marine sedimentary environments. Among the sedimentary processes known in pore fluids, early diagenesis, such as dissolution of iron and manganese oxides in the first tens of centimeters of the seafloor sediment, often lead to a MREE-enriched pattern in pore waters (Haley et al., 2004; Deng et al., 2017). Linear REE patterns are found below the Mn reduction zone (Haley et al., 2004; Kim et al., 2012). At deeper depth, HREE-enriched patterns with a negative Ce anomaly are observable due to the remineralizations of particulate organic matter in the methanogenic zone (Kim et al., 2012). However, such REE records in pore fluids are still geographically scattered and fragmentary, which precludes a complete characterization.

The behavior of REEs and major elements in the pore fluids of turbidite deposits characterized by high sedimentation rates remains poorly constrained, despite their critical role in tracing biogeochemical processes unique to these high-energy depositional systems. Indeed, turbidity currents are efficient in transporting terrigenous sediments and can also transport a large amount of organic matter into the submarine canyons (Martín et al., 2011; Hage et al., 2024; Zhang et al., 2024). The degradation of these organic matters and detrital materials may have a considerable impact on the early diagenesis of sediments and REE fractionations of pore fluids (Haley et al., 2004; Wang et al., 2022). Consequently, further work is needed to constrain the behavior of these specific elements in the fluids of deep-sea sediment cores (Smrzka et al., 2019).

Here, we have systematically analyzed major (Na, Ca, Mg) and trace (Ba, Mn, Mo, U, REEs and Y) element concentrations in pore fluids collected from sediment cores located along the Gaoping and Penghu submarine canyons of the northern South China Sea (SCS). Our results permit us to assess the potential impact of early-diagenesis on the REEs of pore fluids of sediments characterized by relatively high sedimentation rates (from 55 to 560 cm/kyr) in hemipelagic and turbiditic sedimentary environments.

2. Materials and sedimentological settings

Six long Calypso cores and three CAlypso SQuare box (CASQ) cores were collected on the banks of the Gaoping and Penghu submarine canyons during the *HydroSed* cruise, on board *R/V Marion Dufresne*, in June 2018 (Fig. 1, Table 1). Detailed lithology and estimation of sedimentation rates for each core are presented in Table 1 and in Supplementary figs. 1 and 2.

The Gaoping and Penghu submarine canyons transport large amounts of sediments from Taiwanese rivers to the northern SCS during the late Quaternary (Liu et al., 2016; Bertaz et al., 2024). These two submarine canyons are characterized by different land-sea configurations which result in distinct sedimentation rates and lithologies for studied cores located close to each of these two submarine canyons.

The Gaoping Canyon is a very active submarine canyon system connecting the Gaoping River to the deep-sea trench system (Fig. 1). The Gaoping River is characterized by a relatively small and mountainous catchment area with a relatively limited floodplain, delta and shelf (Huh et al., 2009). It has been shown that during typhoon events, the intense rainfall and runoff lead to intense physical erosion and increased sediment discharge by the Gaoping River (Dadson et al., 2003; Zhang et al., 2018). In such conditions, the suspended-sediment concentration of the

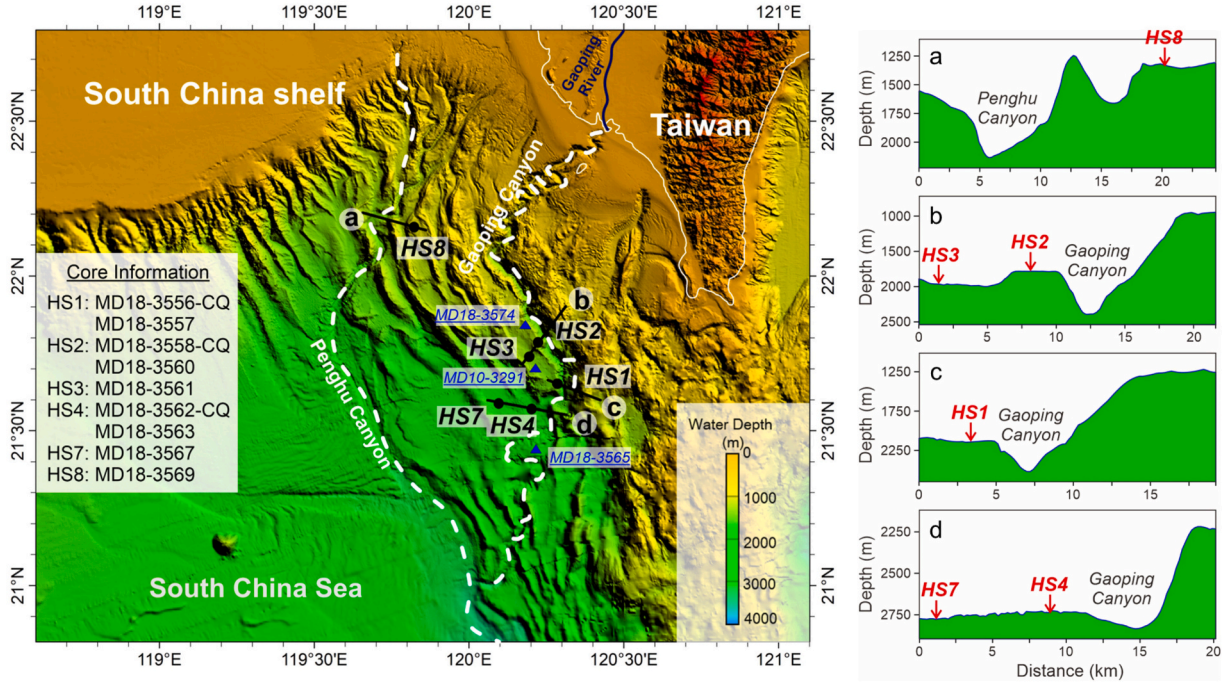

Fig. 1. Bathymetric maps of the northeastern SCS showing the location of studied cores (and site numbers) (black dots) where pore fluids were collected. We also reported four bathymetric profiles indicating the distances and altitudes of studied sites HYDROSED (Sites HS) in relation to the thalweg of the Gaoping and Penghu submarine canyons. The blue triangles represent the sediment cores mentioned in the text (Hu et al., 2017; Huang et al., 2023a; Bertaz et al., 2024). The Gaoping River and the submarine Canyons (Penghu Canyon and Gaoping Canyon) are also displayed. (For interpretation of the references to colour in this figure legend, the reader is referred to the web version of this article.)

Table 1
Detailed sampling information, lithology and estimation of sedimentation rate for studying cores.

Site	Latitude and longitude	Water depth (m)	Estimated sedimentation rate	Core name	Length (m)	Lithology
HS1	21°39.04′ N, 120°16.95′ E	2102	~561 cm/kyr (MD18–3574, Table S1)	MD18–3557	22.7	Dark greenish gray clyey sediment, stacked fine-grained overflow deposite from turbidity currents.
				MD18–3556-CQ	7.1	Dark greenish gray clayed sediment showing numerous mm-scale silty clay to silty laminations.Frequent organic-rich concretions and layers are observed.
HS2	21°46.99′ N, 120°13.17′ E	1793	~561 cm/kyr (MD18–3574, Table S1)	MD18–3560	28.9	Dark greenish gray clayed sediment showing numerous mm-scale silty clay to silty laminations. Frequent organic-rich concretions and layers are observed.
				MD18–3558-CQ	8.1	Dark greenish gray clyey sediment, stacked fine-grained overflow deposite from turbidity currents.
HS3	21°44.31′ N, 120°11.55′ E	1953	~130 cm/kyr (MD10–3291, Yu et al., 2017a)	MD18–3561	40.5	Dark greenish gray clay sediment with silty clay, discoutinuous laminations
HS4	21°34.13′ N, 120°11.98′ E	2711	~510 cm/kyr (MD18–3565, Huang et al., 2023a)	MD18–3563	20.1	Dark greenish gray clay sediment showing countless centimeter to decimeter-scale sandy deposits, turbidites
				MD18–3562-CQ	3.0	Dark greenish gray clay sediment showing countless centimeter to decimeter-scale sandy deposits, turbidites
HS7	21°35.25′ N, 120°05.62′ E	2746	<510 cm/kyr (MD18–3565, Huang et al., 2023a)	MD18–3567	20.1	Dark greenish gray clay sediment showing countless centimeter to decimeter-scale sandy deposits, turbidites
HS8	22°09.30′ N, 119°49.24′ E	1320	54.7 cm/kyr (Bertaz et al., 2024)	MD18–3569	40.1	Very dark greenish clay with some foraminifera

river plume offshore from the Gaoping River and at the head of Gaoping Canyon can be high enough to generate nepheloid layers on the slope and turbulent hyperpycnal flows within the canyon (Zhang et al., 2018). Three and a half years of in situ subsea mooring observations conducted on the levee, approximately 3.5 km laterally and 500 m vertically from the thalweg of the Gaoping Canyon, demonstrate that typhoon-induced turbidity currents are associated with enhanced sediment flux, elevated temperature, and reduced salinity, reflecting the lateral dispersion of turbidity currents onto the canyon bank (Zhang et al., 2018). The lithology of sediments from all investigated cores collected on the banks of the Gaoping submarine canyon is thus mainly composed of a succession of turbidites deposits exhibiting different thickness and grain-size depending mainly from the elevation of the core above the canyon thalweg (Fig. S1, S2). In more detail, Sites HS1 (Cores MD18–3556-CQ and MD18–3557), HS2 (Core MD18–3558-CQ and MD18–3560) and HS3 (Core MD18–3561) in the northern part of the studied area are at altitudes of ~540–650 m above the thalweg of Gaoping submarine canyon (Fig. 1, Table 1). The cores are mainly composed of deposits of silty mud sediments interbedded with thin silty layers with erosive bases corresponding to turbidite deposits with a thickness of between 0.5 and 5 cm (Fig. S1, S2). On the other hand, sites HS4 (Cores MD18–3562-CQ and MD18–3563), and HS7 (Core MD18–3567) are located further south (Fig. 1, Table 1) at lower altitudes above the thalweg of the Gaoping submarine canyon (between 125 and 250 m) and are composed of thicker, coarser turbidite layers from 1 to 20 cm in thickness (Fig. S1, S2). All investigated cores, located on the flat bank of Gaoping submarine canyon, are characterized by slightly variable sedimentation rates reaching up to ~250–560 cm/kyr for studied sites close to the canyon (HS1, HS2, HS4 and HS7), with lower values (~130 cm/kyr) for distal studied sites (HS3), estimated from comparison with proximal cores (Fig. 1, S3, S4, Table 1). The mean sedimentation rate at Sites HS1 and HS2 is estimated by reference to Calypso Core MD18–3574 (21°50.42′N, 120°10.67′E; 22.52 m long; 1171 m water depth), which is located on a similar western levee of the Gaoping submarine canyon to Sites HS1 and HS2 (Fig. 1). The age model for this core is based on 11 calibrated radiocarbon dates and indicates a mean sedimentation rate of 560 cm/kyr (Fig. S3, Table S1). Three calibrated radiocarbon dates obtained on core MD18–3557 (HS1) confirmed a high sedimentation rate for this core (mean sedimentation rate of 510 cm/kyr; Fig. S3, Table S1).

Calypso Core MD18–3561 (Site HS3) is located at a greater distance from the Gaoping submarine canyon than cores at sites HS1 and HS2 and very close to Core MD10–3291 (21°14.49′ E, 120°13.91′ N, water depth of 2070 m) where the mean sedimentation rate has been estimated to be 130 cm/kyr (Yu et al., 2017a, Fig. S4). A comparison of the magnetic susceptibility record of core MD18–3561 with those of the well-constrained chronology of core MD10–3291 allowed us to estimate a mean sedimentation rate of approximately 130 cm/kyr for core MD18–3561 (Fig. S4). The mean sedimentation rate of Site HS4 and HS7 are estimated to be lower than the dated cores nearby which are closer to the canyon thalweg (e.g. mean sedimentation rate of 510 cm/kyr for Core MD18–3565; Huang et al., 2023a).

Calypso Core MD18–3569 was collected at Site HS8 located on the eastern bank of the Penghu Canyon (Fig. 1, Table 1). The lithology of Core MD18–3569 consists mainly of a greenish gray homogenous hemipelagic mud without any visible turbidites (Fig. S1). The mean sedimentation rate of Core MD18–3569 is lower than the other studied sites with a value of ~55 cm/kyr (Bertaz et al., 2024). At present time, the Penghu Canyon is not connected to any rivers flowing from southern China or southern Taiwan. The head of the Penghu Canyon begins at the South China shelf break and sediment sources are either the Taiwan Strait or the rivers of south-western Taiwan (Huh et al., 2011).

3. Methods

3.1. Pore fluids sampling

140 pore fluid samples have been collected from six Calypso and three CASQ cores using precleaned ceramic sticks (*Rhizon*) with vacuum syringes (30–50 cm per sample for CASQ cores and 150 cm per sample for Calypso cores). The volumes of pore fluids samples extracted from sediments were around 10 to 14 ml. Pore fluids samples were filtered and acidified to a pH of less than 2 with supra-pure 6 N HCl and then stored in a fridge at +4 °C to prevent of any effects of evaporation.

CASQ coring permits the upper 10 m to be collected without significant disturbance of the upper part of the sediments (Kissel et al., 2013) which permit us to collected pore fluids samples at high resolution, every 30 cm, along the upper meters of the core. In contrast, the

uppermost layers (upper 150–300 cm) of the Calypso cores can be disturbed by the coring system, but at greater depth they extend the sequence of high-quality sediment to 40 m with sampling depth interval resolution of 150 cm per sample. Thus, combining results of both cores have the potential to provide a unique and fully detailed depth profile of variations in major and trace element concentrations of the upper 40 m of the southern margin of Taiwan. This enables us to study a continuous diagenesis process from the top (seawater - sediment interface) to the bottom.

3.2. Major and trace element concentrations analyses

The concentrations of major elements (Na, Ca and Mg) and trace elements (Ba, Mn, Mo and U) in pore fluids were measured by the *ThermoScientific* Inductively Coupled Plasma Mass Spectrometer (ICP-MS *Xseries*^{II}) of the PANOPLY's analytical facilities at the *Laboratoire des Sciences du Climat et de l'Environnement (LSCE)*, *University Paris-Saclay, France*. To take account of matrix effects due to salt content, samples were systematically diluted by a factor of 400. Calibrations were performed using the standard addition method with NASS-6 diluted 400-fold serving as the charged matrix. During the analytical sequences, blanks, two standard seawater solutions IAPSO and NASS-6 and standard reference solution NIST 1640a were run to verify the ICP-MS calibration obtained from the measurements of primary standard solutions, to correct instrumental drift, to validate the dataset and finally to evaluate analytical uncertainties. Based on the measurement of NASS-6 replicates ($n = 29$), 2σ relative standard deviations were 1.7% for Na, 6.6% for Ba, 2.6% for Mg, 2.8% for Ca, 5.3% for Mo, 2.8% for U. As the Mn value is too low in NASS-6, analytical uncertainty is estimated to be better than 5.3% (2σ) for Mn based on NIST 1640a analyses ($n = 10$).

3.3. REE concentration analyses

REE and Y concentrations have been analyzed on 5 ml aliquots of pore fluids using the *ThermoScientific* MS–iCAP *TQ* of the PANOPLY's analytical facilities at the *Laboratoire des Sciences du Climat et de l'Environnement (LSCE)*, *University Paris-Saclay, France*. The analytical procedure used to extract and purify REEs from the matrix has been adapted from the analytical procedure described in detail by Wu et al. (2015). Briefly, an ultra-pure $FeCl_3$ solution and a spike solution enriched in ^{141}Pr and ^{169}Tm were added to each sample with contents around 10–50 fold higher than REE concentrations in the samples. After 48 h of equilibration under regular shaking, the pH was adjusted to ~8 through the addition of ultraclean NH_4OH (Optima grade), leading to the formation of iron hydroxides, which, in turn, efficiently scavenge REEs out of the pore fluids samples. After a few days of regular shaking, the REE co-precipitated fractions were then separated from the remaining solution through several centrifugations and *Milli-Q* water doped with several drops of a molar NH_4OH solution. During analytical sequences using ICP-MS, REE concentrations were corrected for any sensitivity drift of the machine by using internal standard monitoring. The added ^{141}Pr and ^{169}Tm spikes allowed the calculation of the REE extraction step recovery (higher than 92%) and finally REE concentrations by taking into account the initial Pr and Tm contents in the samples. As ^{151}Eu and ^{153}Eu were affected by Ba—O interferences during ICP-MS analyses, owing to the high Ba concentrations remaining after chemical separation, particularly in the Ba-rich pore fluids from HS1, HS3, and HS8, Eu concentrations are not considered here. The accuracy of calibrations and determination of REE concentrations was verified during the analytical sequences by analysis of the geological standard BCR-2 prepared at various dilutions. Blank corrections were systematically applied for all REEs since analysis of chemical blanks (reagents, spike solutions before and after chemistry, filtration step, etc.) revealed a non-negligible but reproducible REE signal (around ±20%, $n = 3$) with contributions of ~10% for HREE and up to 20%, for LREEs for the pore fluid sample with the lowest concentration of rare earth elements. For most of the pore fluids, such blank corrections were negligible. Finally, our measurements were characterized by analytical uncertainties that were systematically below 15% (2σ) for all REEs. This is illustrated in supplementary fig. S5, which presents REE concentrations measured for the seawater standard NASS-6 using the same analytical procedure as that applied to the pore fluids samples. Such uncertainties integrate the accuracy of ICP-MS calibrations, the addition of a spike solution or other reagents, the filtration step, the Fe-oxide co-precipitation and REE extraction, REE measurement, and, finally, the external reproducibility. In addition, the use of Rhizon samplers for pore-water extraction may influence the measured REE concentrations. Based on repeated blank tests, we estimate that contributions from Rhizon samplers are negligible for MREEs (with the exception of Eu) and HREEs. In contrast, blank experiments conducted under acidic conditions indicate that REE release from Rhizon samplers may reach up to ~1.5–2 pM for La, Ce, and Nd under our analytical conditions. Because these blanks were performed under acidic conditions, they likely overestimate the actual release of La, Ce, and Nd under natural pore-water conditions. Accordingly, we excluded from the dataset all La, Ce, and Nd concentrations below 8 pM to minimize potential bias associated with sampler-derived contamination.

4. Results

4.1. Major and trace element concentrations

The Na concentrations in all the cores range from 9500 to 11,100 ppm with a mean value of 10,450 ± 261 ppm, which is consistent with the expected seawater Na concentration of 10,600 ppm estimated from regional deep salinity of 34.6‰ (Fig. S6, Huang et al., 2023b). To help comparison of both major and trace results throughout all cores, as well as correction for any potential effects of evaporation during storage, all element concentrations were normalized to Na by calculating the (C_i/$[Na]_{sample}$) ratio for each sample and then multiplying this ratio by the average Na concentration ($[Na]_{avg}$) of the entire dataset: $C_{i\text{-normalized}} = (C_i/[Na]_{sample}) \times [Na]_{avg}$. For the upper 500 cm, the major (Ca, Mg) and trace element (Ba, Mn, Mo, U) concentrations measured at higher resolution in CASQ Cores MD18–3556-CQ (Site HS1), MD18–3558-CQ (Site HS2), and MD18–3562-CQ (Site HS4) are consistent with the values measured along the calypso Cores MD18–3557 (Site HS1), MD18–3560 (Site HS2) and MD18–3563 (Site HS4), respectively (Fig. S7). This indicates that results of the major and trace elements in the different sediment sequences are reproducible. Variations in Mo and U concentrations are more evident in the CASQ cores, highlighting potentially rapid changes at the top of the cores. Such variations are less visible in Calypso cores due to the potential for disturbance of the core-top sediment by the coring system.

The Ca concentrations display a systematic drop over the first 800 cm for Cores MD18–3557 (Site HS1), MD18–3561 (Site HS3) and MD18–3569 (Site HS8) (Fig. 2), decreasing from ~9.8 ± 0.03 to ~3 ± 0.01 mM for Ca. This decrease is less marked for Core MD18–3560 (Site HS2). At deeper depth, the Ca concentrations of these cores remain stable. Such trends in Ca concentrations are less pronounced for Cores MD18–3563 (Site HS4) and MD18–3567 (Site HS7), the sediments of which are composed of thicker and coarser turbidite layers (Fig. S1, S2). The Mg concentrations display also a systematic decrease over the first 800 cm which is more or less important (from 50 to ~32–40 mM) in all the studied cores expect Core MD18–3563 (Site HS4) which present relatively constant high Mg concentrations (~50 mM) (Fig. 2). At deeper depth, the Mg concentrations continuous decrease slightly for Cores MD18–3560 (Site HS2), MD18–3561 (Site HS8) and MD18–3567 (Site HS7).

For Cores MD18–3557 (Site HS1), MD18–3561 (Site HS3) and MD18–3569 (Site HS8), Ba displays relatively low concentrations (nearly zero) in the upper 600–800 cm depth, and abruptly increases to over 20,000 nM downward. A similar trend in pore fluids is observed at

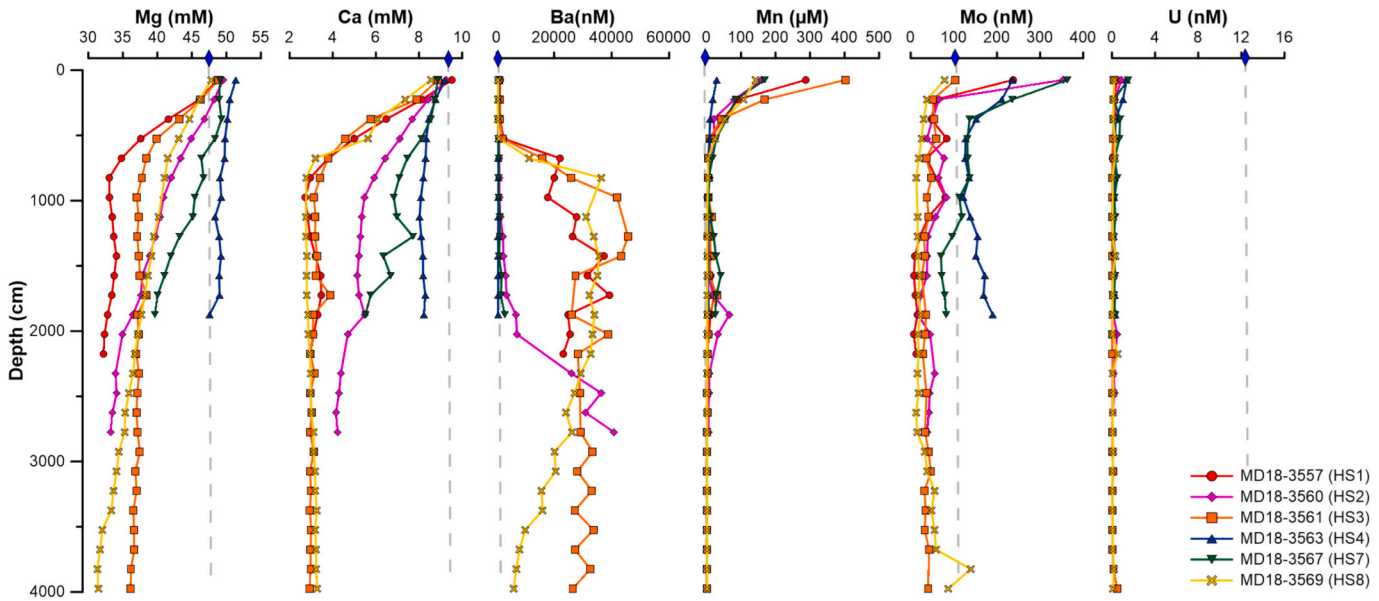

Fig. 2. Major (Mg and Ca) and trace element (Ba, Mn, Mo and U) concentration profiles with depth obtained in pore fluids of Calypso Cores MD18–3557 (Site HS1), MD18–3560 (Site HS2), MD18–3561 (Site HS3), MD18–3563 (Site HS4), MD18–3567 (Site HS7) and MD18–3569 (Site HS8). The values of deep water (NASS-6) are indicated by blue diamonds, and the gray dashed line represents a seawater baseline. (For interpretation of the references to colour in this figure legend, the reader is referred to the web version of this article.)

greater depth (around 2000 cm) in Core MD18–3560 (Site HS2). Very low Ba concentrations are observed all along Cores MD18–3563 (Site HS4) and MD18–3567 (Site HS7) (Fig. 2).

Except for the Calypso core MD18–3563 (Site HS4), Mn concentrations decrease from more than 300 μM at top 30 cm to nearly 0 at ~300 cm depth and then stay constant at deeper depth in all the cores (Figs. 2 and 3). The abrupt decrease is observed at shallower depth (around 100 cm) for CASQ Core MD18–3562-CQ (Site HS4) whereas no significant changes are recorded for the upper part of the Calypso Core MD18–3563 (Site HS4).

Variations of Mo concentrations decrease in Calypso Cores MD18–3557 (Site HS1), MD18–3560 (Site HS2), MD18–3561 (Site HS3) and MD18–3569 (Site HS8) from more than 300 nM at 75 cm to lower values around 300 cm. This decrease is observed at slightly greater depth (500 cm) for Cores MD18–3563 (Site HS4) and MD18–3567 (Site HS7). Higher resolution analyses in the upper part of CASQ cores indicate an increase from 100 nM in the core top (similar to seawater value) to a maximum (around 300 nM) at 100 cm for Cores MD18–3556-CQ (Site HS1) and MD18–3558-CQ (Site HS2) and at 100 to 200 cm for Core MD18–3562-CQ (Site HS4) (Fig. 3).

Variation in U concentrations is observed in the upper few tens of centimeters of the CASQ cores, which results in a rapid decrease from ~12 nM at the surface to nearly 0 at 70–80 cm (Fig. 3). The Calypso cores do not display a decrease of U concentrations because of the low-

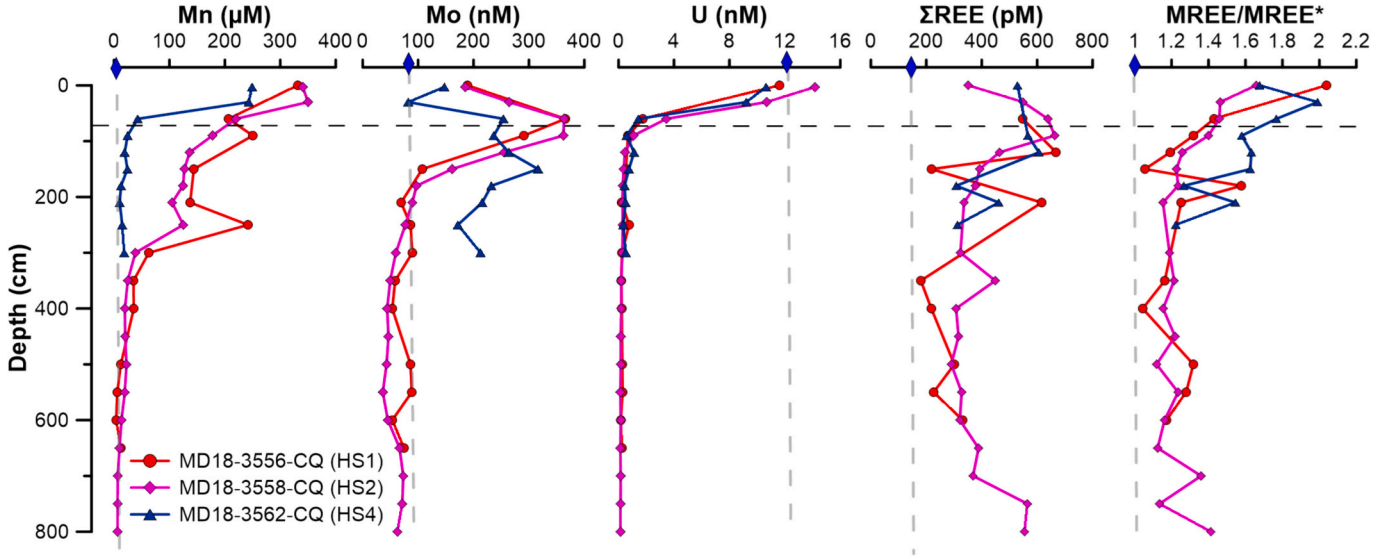

Fig. 3. Mn, Mo, U and ΣREE concentrations and MREE/MREE* ratio variations with depth obtained in pore fluids of CASQ Cores MD18–3556-CQ (Site HS1), MD18–3558-CQ (Site HS2) and MD18–3562-CQ (HS4). The values of deep water (NASS-6, Site HS1 for REE results, Huang et al., 2023b) are indicated by blue diamonds and the gray dashed line represents a seawater baseline. (For interpretation of the references to colour in this figure legend, the reader is referred to the web version of this article.)

resolution sampling in the sub-surface and possible perturbation of sediments of the upper cores due to the coring system (Fig. 2).

4.2. Rare earth element concentrations

To avoid the Oddo-Harkins effect (Schmitt et al., 1963) and to plot their patterns, the REE concentrations in pore fluids are commonly normalized to the Post Archaean Australian Shale (PAAS; McLennan, 2001). The calculated MREE/MREE* values ($[Gd_N + Dy_N]/[Yb_N + Nd_N]$ ratio; Yu et al., 2017b; Huang et al., 2023b) are also used to identify the fractionation between HREE (Ho, Er, Tm Yb, Lu), LREE (La, Ce, Pr, Nd) and MREE (Sm, Gd, Tb, Dy).

Total REE concentrations (ΣREE), and MREE/MREE* of pore fluid samples are reported in Figs. 3, 4. Two types of ΣREE depth profile are observed for the investigated cores. The first one is the gradual downward decreasing trend in ΣREE visible in upper 500 to 700 cm of Cores MD18–3557 (Site HS1), MD18–3560 (Site HS2), MD18–3563 (Site HS4) and MD18–3567 (Site HS7) with several peaks of ΣREE at a greater depth. The REE concentrations are high in the upper 100 cm of the cores (400–800 pM). Such values are three- to four-times higher than the mean values measured in deep waters collected at the closet water station Site HS1 (ΣREE of 150 pM; Huang et al., 2023b). A decrease to a relatively low value (200 pM) is observed at around 500–700 cm. The second type of depth profile is observed in the longest Cores MD18–3561 (Site HS3) and MD18–3569 (Site HS8). For these cores, relatively low ΣREE values (100–200 pM), similar to seawater values (blue diamonds reported in Fig. 4), are observed in the upper section of the cores. For Core MD18–3569 (Site HS8), the ΣREE values increase to 380 pM at ~500 cm depth and remain high down to the bottom of the core. For Core MD18–3561 (Site HS3), an increase in ΣREE concentrations up to 920 pM is observed at 3500 cm. The MREE/MREE* ratios in Cores MD18–3557 (Site HS1), MD18–3560 (Site HS2), MD18–3561 (Site HS3) and MD18–3569 (Site HS8) show a decreasing trend downward, while in Cores MD18–3563 (Site HS4) and MD18–3567 (Site HS7), several increases of MREE/MREE* at deep depth are observed to be coupled with rising ΣREE concentrations.

5. Discussion

The studied pore fluids were collected in sedimentary environments characterized by relatively high sedimentation rates (between 55 and 560 cm/kyr; Table 1; Fig. S3) and contrasted lithologies: coarse and thick turbidite sequences (Sites HS4 and HS7; Supplementary Table 1), very fine and thin turbidite sequences (Sites HS1, HS2, HS3; Supplementary Table 1) and hemipelagic deposits (Site HS8, no turbidites deposits, Supplementary Table 1) (Figs. S1 and S2). Metal element concentrations of pore fluids samples from all the cores vary greatly with depth and reflect the diagenesis process of sediments. In the following sections, we firstly discuss the processes that dominate the REE fractionations downward from the sediment–seawater interface and then we discuss the potential influence of turbidite layers on the REE fractionations of pore fluids.

5.1. Redox sensitive elements at sediment top

Most metal elements are directly or indirectly affected by changing redox conditions driven by the action of microbial respiration (Paul et al., 2019a; Smrzka et al., 2019). The concentration of the elements Mn, Mo, U in the upper pore fluids samples (Figs. 2 and 3), well observed in CASQ cores, is closely associated with the reduction-oxidation (redox) transition, which implies a depletion of oxygen as a result of organic matter degradation in the upper tens of centimeters.

In the pore fluids, dissolved Mn is generally present in Mn(II) and Mn (III) states, as obtained by the reductive dissolution of Mn oxides coupled with the decomposition of organic matter in the suboxic environment (Froelich et al., 1979). The high Mn concentration in the upper 50 cm of all the cores is thus linked to the reduction of Mn oxides in the oxygen- deficient environment (Fig. 3). Notably, Core MD18–3562-CQ (Site HS4) reveals a sharp Mn drop to nearly zero at around 100 cm, while the other two CASQ cores decrease gradually to reach nearly zero

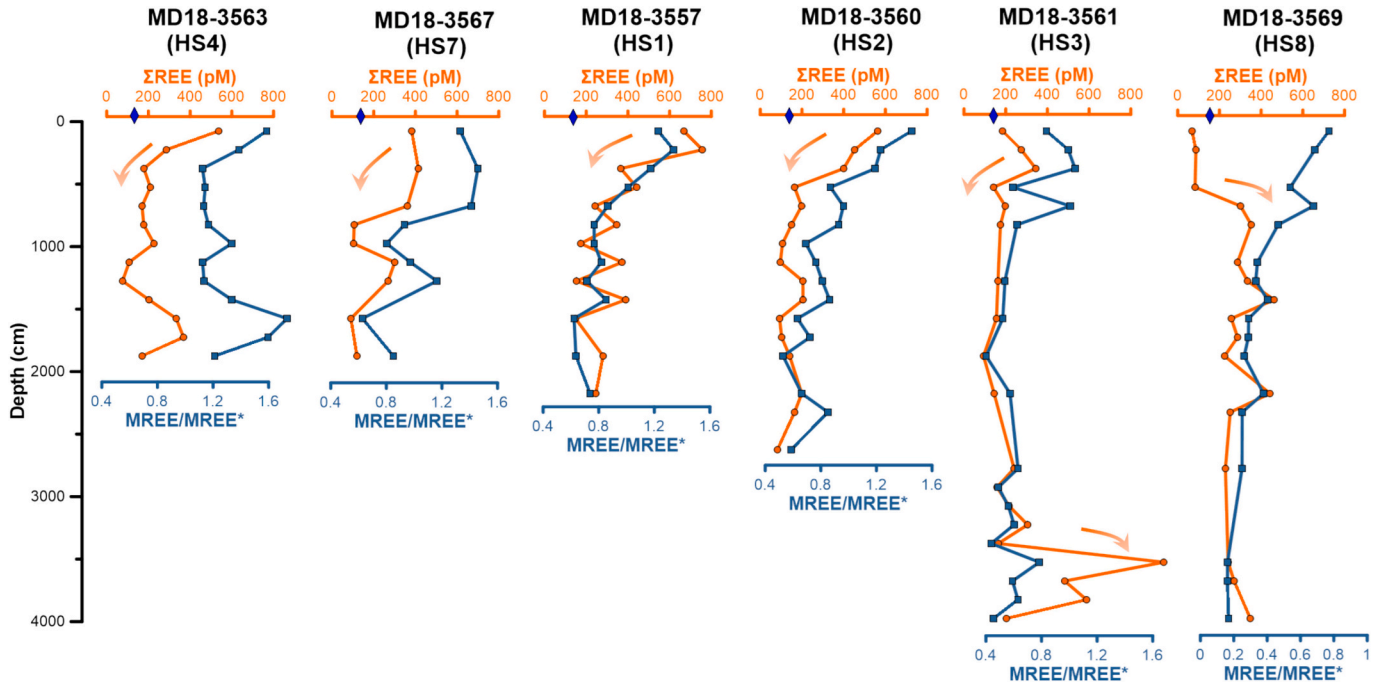

Fig. 4. ΣREE concentrations and MREE/MREE* ratio variations with depth obtained in pore fluids of Calypso Cores MD18–3557 (Site HS1), MD18–3560 (Site HS2), MD18–3561 (Site HS3), MD18–3563 (Site HS4), MD18–3567 (Site HS7) and MD18–3569 (Site HS8). The cores are shown, from left to right, from turbidite deposits with thicker and coarser grain-size turbidite layers to less thick and finer grain-size turbidite layers, according to the lithology. Core MD18–3569 (HS8) located on the right side corresponds to hemipelagic sediments mainly composed of homogenous hemipelagic mud without any visible turbidites. Simplified lithology of each site is shown besides the curves. Arrows along the curve indicates the decreasing/increasing trend.

at around 300 cm.

Similarly, the elements U and Mo are sensitive to oxygen concentrations (Yano et al., 2020). Within the oxygenated pore fluids, U is found as soluble U (VI) (Calvert and Pedersen, 1993), but as the oxygen content is rapidly depleted with depth, soluble U (VI) will reduce to insoluble U (IV) and precipitate as an authigenic solid (Anderson, 1982; Owens et al., 2011). Thus, a low U concentration in pore fluids, can be used as a qualitative indicator of low oxygen content (Costa et al., 2023). The decreasing trend in the upper 80 cm of all the CASQ cores implies a decrease of oxygen concentration until a redox interface that resides at a depth of approximately 80 cm for sites HS1, HS2 and HS4 (Fig. 3).

The minimum U concentration has been observed to correspond with the maximum of Mo concentration. As Mo fixation requires the availability of hydrogen sulphide (Scholz et al., 2014), thus the decrease of Mo concentration occurs deeper depth than U concentration in Cores MD18–3556-CQ (Site HS1), MD18–3558-CQ (Site HS2) and MD18–3562-CQ (Site HS4) (Fig. 3). This is in agreement with several previous studies showing the association of Mo enrichment with lower redox potentials and high sulfide concentrations in pore fluids (e.g., Algeo and Lyons, 2006; McManus et al., 2006; Smrzka et al., 2019). For Core MD18–3562-CQ (Site HS4) which is composed of thicker and coarser turbidites sequences, Mo concentration does not greatly decrease until 300 cm. This indicates a deeper depth of occurrence of a sulfidic environment.

The ΣREE concentrations are higher (>350 pM) in the upper 100 cm of cores located along Gaoping canyon (MD18–3563 (Site HS4), MD18–3567 (Site HS7), MD18–3557 (Site HS1) and MD18–3560 (Site HS2)) (Figs. 3, 4). These elevated ΣREE concentrations in the upper 100 cm are associated with MREE/MREE* values consistently greater than 1 (Figs. 3, 4). This could be attributed to the selective release of MREEs into fluids via the reduction of Fe—Mn oxyhydroxide (Mn oxides more likely than Fe oxides) in the subsurface, as MREEs exhibit a particular affinity for manganese oxides (Haley et al., 2021; Hatje et al., 2024). The ΣREE peak and higher MREE/MREE* in the core top of 100 cm coincides with the high concentrations of dissolved Mn in the subsurface (R^2 of 0.84, 0.81 and 0.41 between MREE/MREE* and Mn concentration for the upper 200 cm of sediments from Cores MD18–3556-CQ (Site HS1), MD18–3558-CQ (Site HS2) and MD18–3562-CQ (Site HS4) (Fig. S8), with lower coefficient of correlation for site HS4 which is strongly influenced by the turbidity current. This is also in agreement with the previous studies demonstrating that MnO_2 could be the main source of REE for pore fluids (Du et al., 2025). This observation supports common redox effects on REE distribution in pore fluids in the upper part of the core from the southern margin of Taiwan. Results indicate that a potential flux from sediments preferentially releases MREEs to the pore fluids at these depths and could account for the increased ΣREEs, MREE/MREE* of bottom water at the studied site (HS1, Fig. S9; Huang et al., 2023b).

5.2. *Sulfate reduction and the methanogenesis process and their impact on REE fractionation in pore fluids*

The solid phase of barium, barium sulfate (barite), is known to be stable in undersaturated waters (Paytan and Griffith, 2007) and its precipitation in seawater should be thermodynamically unfavorable. Thus, the barium concentrations in the seawater and in the pore fluids in the upper several meters of our studied cores are very low (Fig. 2). At deeper depth, in a context of low oxygen concentrations, pore fluids sulfate can act as an oxidant for anaerobic respiration which allows the dissolution of barite (Breymann et al., 1992; Costa et al., 2023). Consequently, the solubility of barite increases drastically when pore fluids are depleted in sulfate. As a result, the dissolution of barite leads to an increase with depth in the concentration of dissolved Ba in pore fluids by up to four orders of magnitude (von Breymann et al., 1990). This dissolution is primarily driven by sulfate reduction, often occurs at the sulfate-methane transition zone (SMTZ) (Borowski et al., 1996; Snyder et al., 2007), where sulfate is consumed by anaerobic oxidation of methane (AOM: $CH_4 + SO_4^{2-} \rightarrow HCO_3^- + HS^- + H_2O$) and organoclastic sulfate reduction (SR: $2(CH_2O) + SO_4^{2-} \rightarrow 2HCO_3^- + H_2S$) (Borowski et al., 1996). Given the similar sedimentation rate in Cores MD18–3561and MD10–3291 (Fig. S3, S4), the abrupt increase in Ba at 500 cm depth in Core MD18–3561 (Site HS3) is consistent with the increase of CH_4 and DIC, as well as the depletion of SO_4^{2-} in the pore fluids of Core MD10–3291, located close to the studied core (Fig. 6; Hu et al., 2017, Chuang et al., 2019), reflecting comparable geochemical signals at equivalent chronological horizons. Thus, from the variations of Ba concentrations, the SMTZ depth should be located at around 500–600 cm in Cores MD18–3557 (Site HS1), MD18–3561 (Site HS3) and MD18–3569 (Site HS8). The SMTZ is observed at around 2000 cm in Core MD18–3560 (Site HS2) whereas in Cores MD18–3563 (Site HS4) and MD18–3567 (Site HS7) composed of thicker and coarser turbidites sequences, it does not occur above a depth of 2000 cm (Fig. 2).

In calypso Cores MD18–3557 (Site HS1), MD18–3560 (Site HS2), MD18–3561(Site HS3) and MD18–3569 (Site HS8), the concentrations of Ca and Mg in the pore fluids gradually decrease toward the SMTZ in the upper 800 cm of the cores and stay relatively constant at greater depth. The decrease in Ca concentration in the upper meters of Core MD18–3561 (Site HS3) corresponds to the decrease in sulfate and increase in DIC of Core MD10–3291, located very close to Core MD18–3561 and on the same flat bank of Gaoping submarine canyon (Figs. 1 and 6). This suggests that Cores MD18–3561 (Site HS3) and MD10–3291 might be controlled by the same mechanisms. Since sulfate reduction is responsible for the increase in alkalinity, which favors the precipitation of carbonate (Paul et al., 2019b), the simultaneous decrease across the SMTZ of Ca and Mg in Cores MD18–3557 (Site HS1), MD18–3560 (Site HS2), MD18–3561 (Site HS3) and MD18–3569 (Site HS8) could be explained by consumption of both ions for carbonate precipitation (Mg-rich calcite or simultaneous dolomite and calcite formation) at the SMTZ. This is supported by higher ion activity product (IAP, Moore et al., 2004; Wehrmann et al., 2011) more than a constant solubility product (Ksp) of dolomite for all the cores, suggesting favorable conditions for dolomite formation, which then results in the uptake of Mg and Ca from the pore fluids (Fig. S10). Previous studies also found the presence of dolomite rimmed by ankerite and Mg-rich calcite in core MD10–3291 offshore SW Taiwan (Hu et al., 2017). In contrast, the decrease in Ca and Mg is not observed in Core MD18–3563 (Site HS4) and is relatively weak in Core MD18–3567 (Site HS7), which may reflect limited sulfate reduction and minor formation of authigenic carbonates in these cores. However, direct measurements of sulfate gradients are required to confirm this interpretation. This hypothesis is in agreement with the deeper depth of sulfate depletion suggested by the Ba variations in the pore fluids of these cores. Considering that both cores are characterized by the deposition of coarser (high sand proportion) and thicker turbidites (Fig. S1, 2), it seems that the strong turbidite deposits might indeed inhibit the sulfate reduction process and the precipitation of authigenic carbonates.

Below the SMTZ, Mg concentrations in Cores MD18–3560 (Site HS2) and MD18–3569 (Site HS8) continuously decrease with depth, while Ca remains constant. This decoupled behavior cannot be explained by carbonate precipitation alone, which typically affects both Ca and Mg simultaneously. Instead, it may indicate the authigenesis of Mg-rich silicate minerals, such as clays (e.g., Hu et al., 2025), a process often associated with reverse weathering that consumes alkalinity and cations.

The depth profiles of the ΣREE concentrations are different in the two contrasted lithologies of the sediment cores investigated in this study. Indeed, ΣREE concentrations appear a decreasing trend in the upper 800 cm and the concentrations are relatively low (< 200 pM) at deep depth in all cores characterized by turbidite deposits, whereas hemipelagic sediments (Core MD18–3569, Site HS8) are generally associated with increasing concentrations (Fig. 4). The decreasing trend in ΣREE of pore fluids could be related to authigenesis during early

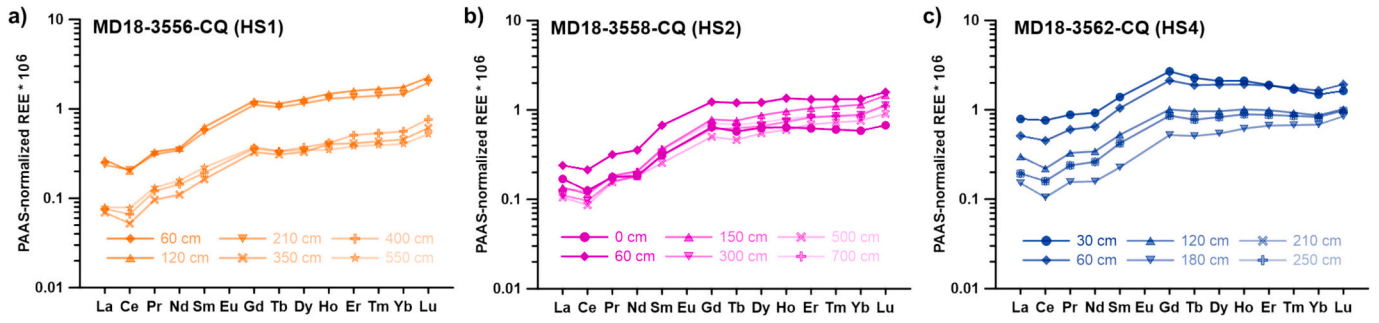

Fig. 5. PAAS-normalized REE patterns of pore fluids in CASQ Cores MD18–3556-CQ (Site HS1) (a), MD18–3558-CQ (Site HS2) (b) and MD18–3562-CQ (Site HS4) (c).

diagenesis (e.g., the reverse weathering process, authigenic clay formation or buried to authigenic phosphate, Du et al., 2022). The PAAS-normalized REE patterns indicate that only samples at the subsurface exhibit an expected MREE enriched pattern in Cores MD18–3556-CQ (Site HS1) and MD18–3562-CQ (Site HS4) (Fig. 5a, c), which is associated with the release of Mn oxides at the redox transition zone as discussed above. The REE patterns of the upper 700 cm present a similar LREE-depleted pattern in all the CASQ cores (Fig. 5a, b, c) and in the upper 600 cm of Core MD18–3569 (Site HS8, Fig. 7a). These REE patterns of pore fluids exhibit a uniform distribution to seawater in Site HS1 (Huang et al., 2023b), with a significantly weaker negative Ce anomalies compared to overlying seawater (Fig. S8). These suggest that the REE pattern of pore fluids mainly preserve a seawater HREE-enriched signature and not greatly impacted by the early diagenesis of sediment during the sulfate reduction process.

ΣREE concentrations in Core MD18–3569 (Site HS8) exhibit a different trend compared to the other cores, as they show a low concentration in the first 600 cm (mean of 77 pM) before increasing abruptly to more than 300 pM by 675 cm (Fig. 4). This rise in ΣREE concentrations is observed in the methanogenic zone below the SMTZ and is coupled with a decreasing trend of MREE/MREE*(Fig. 4). In addition, the PAAS-normalized REE patterns display a significant enrichment of HREE (La/Yb < 0.1) at deeper depth (>600 m) in Core MD18–3569 (Site HS8) and MD18–3561 (Site HS3) (Fig. 7, 8b). This HREE-enrichment pattern was also observed in pore fluids of the northern Cascadia accretion margin in the methanogenic zone, where it has been suggested that HREEs are released during particulate organic carbon (POC) degradation and subsequent chelation by DOC (Kim et al., 2012). Organic matter is expected to have a short residence time in the sulfate-bearing sections of the sediment sequence due to the relatively

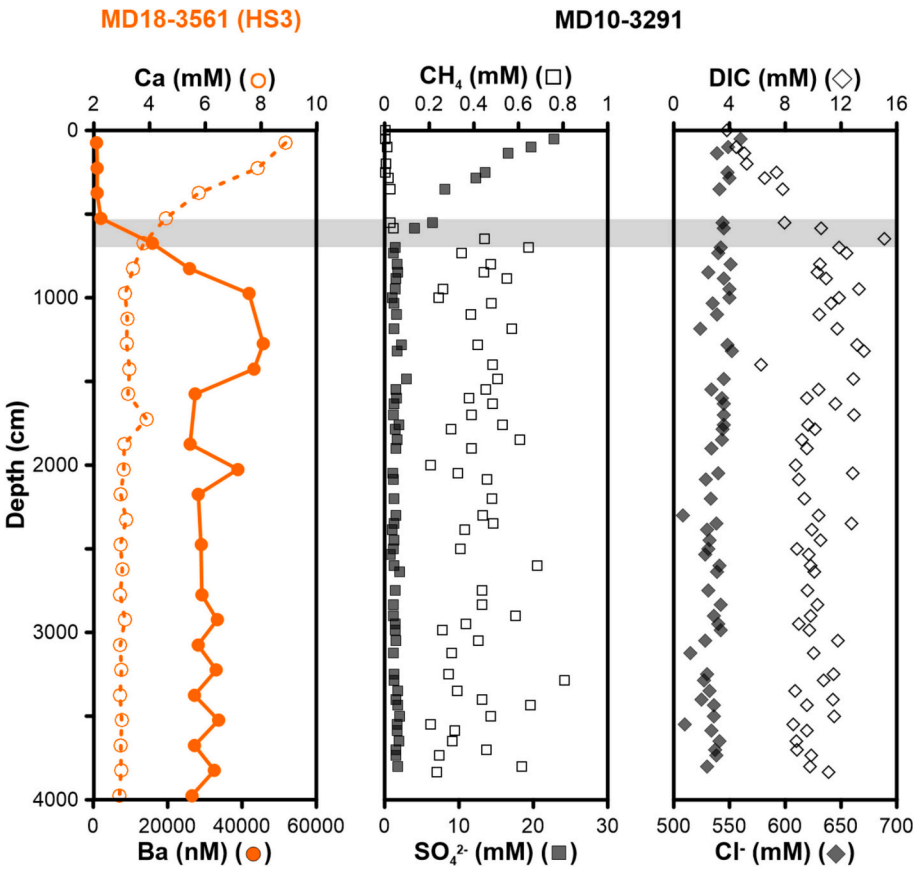

Fig. 6. Depth profiles of Ca and Ba concentrations of pore fluids in Calypso Core MD 18–3561 (Site HS3) compared with depth profiles of dissolved CH_4, SO_4^{2-}, DIC and Cl^- in Core MD10–2393 (Hu et al., 2017). The Sulfate Methane Transition Zone (SMTZ) depths are represented by the horizontal gray bar.

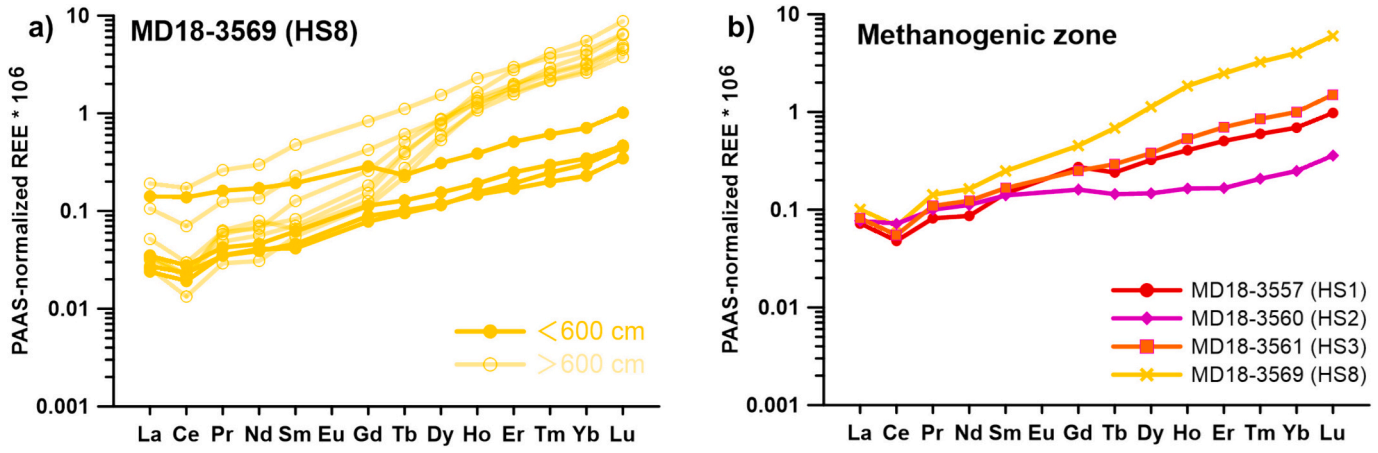

Fig. 7. a) PAAS-normalized REE patterns of pore fluids in Calypso Core MD18–3569 (Site HS8). b) PAAS-normalized REE patterns of pore fluids in methanogenic zone in Core MD18–3557 (Site HS1), MD18–3560 (Site HS2), MD18–3561 (Site HS3) and MD18–3569 (Site HS8).

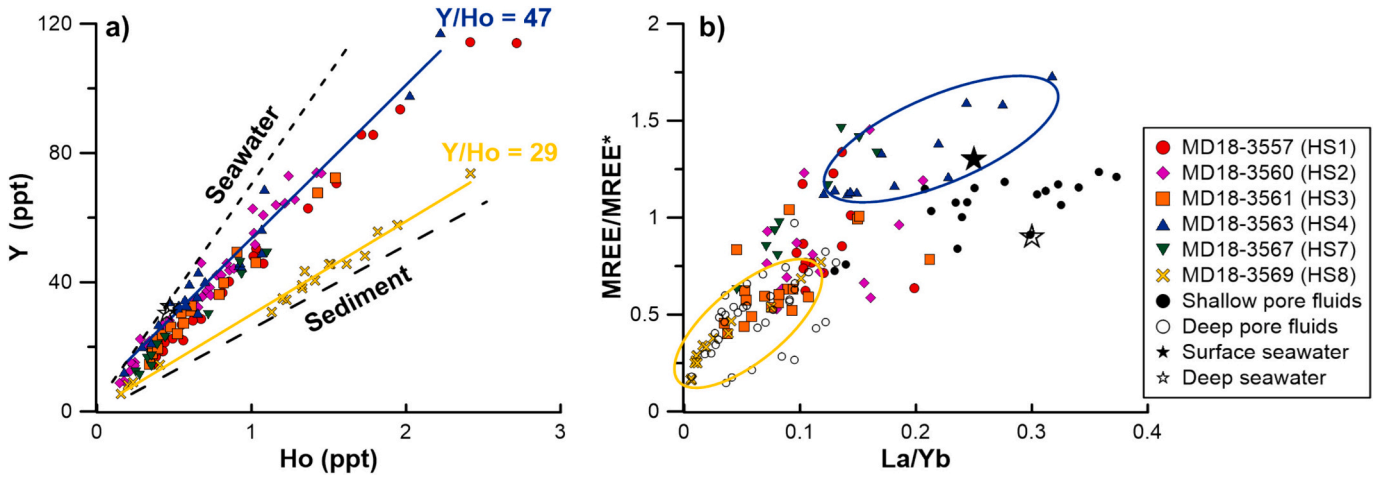

Fig. 8. a) Y concentration versus Ho concentration; b) MREE/MREE* versus La/Yb ratios in all the pore fluids of the studied Calypso cores. Calypso cores from different sites are labeled in different colors. Dashed line in (a) represent the average Y/Ho ratio in seawater (Alibo and Nozaki, 1999) and sediments in the northern South China Sea (Liu et al., 2010). Solid and outlined stars represent the values of surface and deep seawater in Site HS1 (Huang et al., 2023b). Solid circles in (b) show the shallow pore fluids in East China shelf (Deng et al., 2022), the outlined circles represent the deep pore fluids collected in the northern Cascadia accretionary margin (Kim et al., 2012).

high sedimentation rate in Core MD18–3569 (Site HS8, ~55 cm/kyr). This condition may promote the down-core transfer and subsequent release of REEs within the deeper methanogenic zones. Conversely, the lack of pronounced HREE enrichment in turbidite-dominated cores (Fig. 8b; e.g., Cores MD18–3562 (Site HS4) and MD18–3567 (Site HS7)) could be consistent with lower bioavailability of organic matter typically associated with these coarser, often reworked deposits (Hage et al., 2024). More information is needed about the organic matter content in these cores in order to further constrain this hypothesis. Overall, our results support the hypothesis that the POC degradation within the methanogenic zone below the sulfate-reducing zone may play a significant role in the REE enrichment of pore fluids at greater depths (from ~1000 to ~4000 cm) as well as in specific REE partitioning.

It is worth noting that, at a depth greater than ~1000 cm, a few peaks of REE concentrations are visible in Core MD18–3563 (at around 1000 cm, 1500–1800 cm, Site HS4), Core MD18–3567 (1000–1500 cm, Site HS7), and below 3000 cm in Core MD18–3561 (Site HS3) (Fig. 4). Each rise in ΣREE concentration is accompanied by an increase of MREE/MREE*, suggesting a preferential release of MREEs into the pore fluids. Considering the higher content of turbidites in these cores (Fig. S1, S2), we attribute the REE variations at depth along sediment cores to the detrital material delivered by turbidite deposition.

5.3. Impact of turbidites on the REE concentrations in pore fluids

We compare the Y and Ho concentrations in Fig. 8a. The super-chondritic Y/Ho ratio was identified (value of 47) in all cores characterized by turbidite deposit sequences: this ratio is similar to seawater values (Y/Ho ratios range from 47 to 77; Alibo and Nozaki, 1999; Bau and Dulski, 1999). Conversely, pore fluid samples from Core MD18–3569 (Site HS8) characterized by hemipelagic deposit display a significantly different chondritic Y/Ho ratio (mean Y/Ho ratio of 29). This value is comparable to Y/Ho ratios found in surface sediments in the South China Sea (Y/Ho ratio range from 26.1 to 27.2; Liu et al., 2010), and in pore fluids in the central equatorial Pacific (31.6; Paul et al., 2019b). In general, the super-chondritic Y/Ho ratios in seawater are associated with the scavenging process within the water column (Nozaki et al., 1997) as the Ho is more strongly complexed than Y on the surface of particulate matter during the scavenging process (Bau et al., 1997). Thus, it is reasonable to hypothesize that the higher Y/Ho ratios

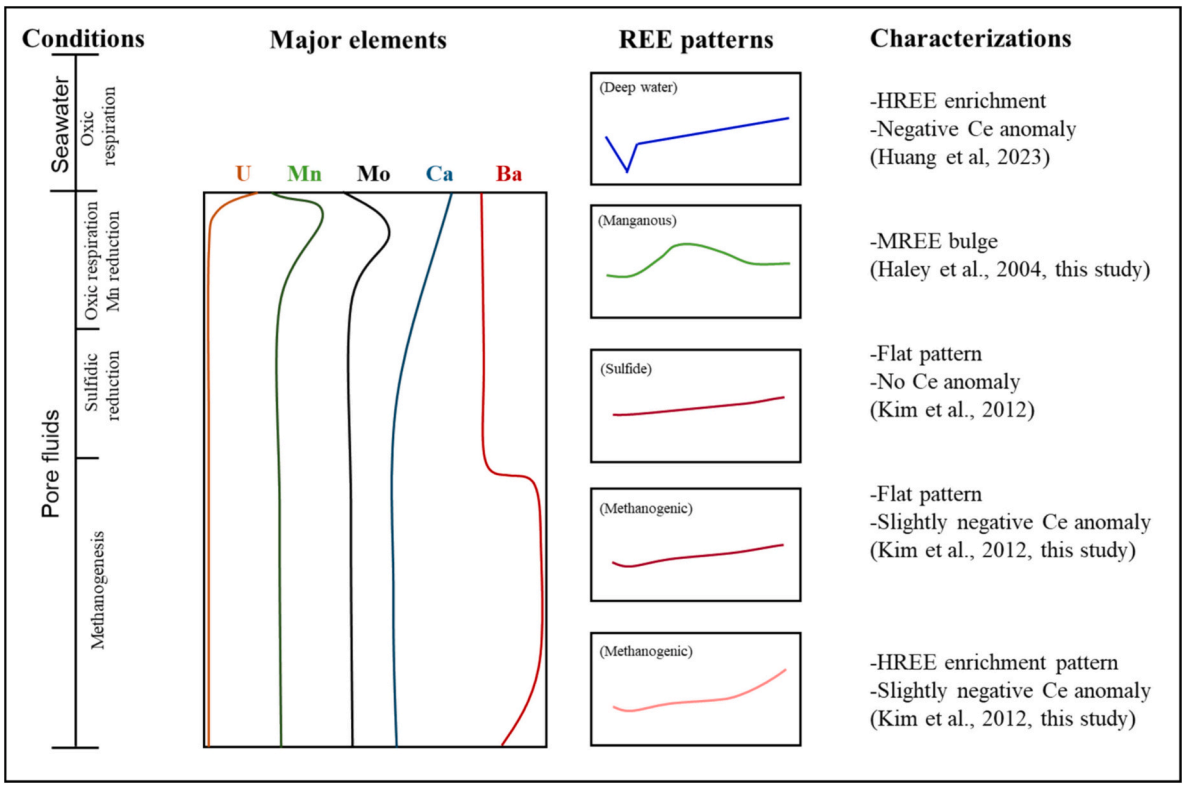

Fig. 9. Pore fluids REE biogeochemical model for the northern South China Sea. The PAAS-normalized REE patterns of sediment pore fluids from Haley et al. (2004) and Kim et al. (2012) have been adapted to this study.

of pore fluids for all the cores along the Gaoping Canyon result from stronger scavenging by coarser fractions in the turbidity currents (Zhang et al., 2018). In addition, the turbidity currents induce significant bottom erosion and perturbation of pore water, remobilizing the REE distributions of pore fluids via strong mixing with seawater.

The high MREE/MREE* (1.6, Fig. 8b) ratios in Core MD18–3563 (Site HS4) are much higher than that of deep water (0.9; Huang et al., 2023b), and more comparable to the values obtained for surface water (1.3; Huang et al., 2023b) from HS1, the closest water station in the SCS, which are greatly impacted by the discharge of detrital material from Taiwanese rivers. As turbidity currents efficiently transport the detrital material to the deep canyon (Zhang et al., 2024), degradation of detrital material and associated organic matter is expected to release more MREEs and LREEs to the pore fluids, leading to higher MREE concentration and La/Yb ratios in Core MD18–3563 (Site HS4). Such REE fractionation of pore fluids in the turbidite deposits is comparable with shallow pore fluids (less than 25 cm bsf) in the East China Shelf (Deng et al., 2022), while REE distributions in Core MD18–3569 (Site HS8) agree with deep pore fluids in the northern Cascadia accretionary margin (Kim et al., 2012) (Fig. 8b). In summary, the turbidity currents create of an extensive, transient redox front due to the rapid burial of reactive organic matter and oxidants by turbidite layers. This non-steady transport process can simultaneously shift the biogeochemical environment and greatly influence the REE distributions of pore fluids at deep depth. Thus, the REE concentrations of pore fluids are definitively dominated by scavenging of terrigenous sediments delivered by the turbidity current and by strong mixing with the overlying seawater in the turbulent environment.

5.4. *Implications of REE fractionations of pore fluids in the northern SCS*

We have summarized the variations of major elements and REE patterns, and drawn an interpretive zonation in Fig. 9. According to the REE models provided by Haley et al. (2004) and Kim et al. (2012), each stage of PAAS-normalized REE patterns and associated sediment diagenesis processes is well observed in our pore fluids collected in cores along the Gaoping and Penghu submarine canyons. The considerable terrigenous inputs from South Taiwanese rivers and transported through the Gaoping Canyon induce high sedimentation rates and a thick redox zone, especially in the sites located in the northern Gaoping Canyon (Sites HS1, HS2 and HS3) and close to the levee (Site HS4). For instance, the MREE enrichment pattern can be recognized even 30 cm below the seafloor in Core MD18–3562-CQ (Site HS4), indicating that the Mn reduction zone can extend to a deeper depth in turbidite deposits. This could be caused by the rapid burial of organic matter which limits its oxidation near the sediment-water interface. This depth is deeper compared to previous pore fluids results from low energy setting, e.g., Buzzards Bay, off the east coast of North America (Sholkovitz et al., 1989), the California margin and the Nazca Ridge off Peru (Haley et al., 2004), the Oregon slope (Abbott et al., 2015) and the Western Pacific (Abbott, 2019), where the Mn reduction zone extends just a few centimeters below the seafloor. The higher REE concentrations related to Mn oxides dissolution have the potential to influence bottom water REE concentrations and patterns. Our data show that diagenetic reactions are confined to the upper 50 cm, which are consistent with previous studies estimating the zone of early diagenesis and its associated benthic flux (Patton et al., 2021; Deng et al., 2022; Du et al., 2022).

A gradual decrease of Ca, Mg and REEs concentrations in pore fluids is associated mainly with adsorption via the formation of authigenic carbonate. This process can extend down to around 800 cm below seafloor in most sites, although it does not appear to induce a notable fractionation of REEs. A significant increase of HREEs in the pore fluids is found at Site HS8, which is interpreted as resulting from POC degradation during the methanogenesis process under sulfate reduction zone. In addition, a Ba decrease is observed below 2500 cm in Site HS8 and, in parallel, methane gas has been observed in core MD18–3569 during onboard investigation, suggesting potential methane seepage in Site HS8. While the REE behaviors are not significantly changed below 2500

cm. More investigation on the presence of gas and organic matter in Core MD18–3569 (Site HS8) and in other cores is needed to further constrain the REE behaviors in the methanogenic zone.

6. Conclusion

We have analyzed the major (Na, Ca and Mg) and trace elements (Ba, Mn, Mo, U, REE and Y) of pore fluid samples from Calypso and CASQ cores retrieved from the turbidity system of the southern margin of Taiwan (sediment banks of the Gaoping and Penghu submarine canyons). The aim was to identify the sediment diagenesis processes in cores characterized by high sediments rates and by the frequent occurrence of thin or thick turbidites deposits, and to assess their potential influence on the REE behavior in pore fluids. The main conclusions of this work are as follows:

1) The dissolution of Mn oxides occurred in the redox transition zone (i.e., in the upper few tens of centimeters below the seafloor) and is associated with a pattern of MREE-enriched pore fluids. Redox diagenesis also affects U and Mo concentrations in the upper part of sediment cores. This early diagenesis of sediments releases REEs to the surrounding pore fluids and has the potential to induce a benthic flux which has modified the REEs pattern and concentrations of the surrounding deep-water masses of the northern South Chine Sea.
2) Decreases in Ca and Mg concentrations in the pore fluids in the upper 800 cm, are probably associated with the formation of authigenic carbonate during the sulfate reduction process. This does not cause a fractionation of REEs. The process of methanogenesis under the SMTZ, recognized here by a pronounced increase in Ba in hemipelagic sediment along the Penghu submarine canyon, contributes to HREE enrichment in the pore fluids.
3) The super-chondritic Y/Ho ratios of pore fluids in all cores characterized by turbidite deposits along the Gaoping submarine canyon, suggest intensive mixing of pore fluids and seawater and stronger reverse-scavenging of detrital materials in the turbiditic sediment sequence system. Large inputs of terrigenous material delivered by the turbidity current cause MREE enrichment and higher La/Yb ratios in the pore fluids from turbidites.

CRediT authorship contribution statement

Yi Huang: Writing – review & editing, Writing – original draft, Methodology, Investigation, Formal analysis, Conceptualization. **Eric Douville:** Writing – review & editing, Methodology, Investigation, Formal analysis. **Christophe Colin:** Writing – review & editing, Supervision, Resources, Data curation, Conceptualization. **Zhifei Liu:** Writing – review & editing, Resources. **Bin Li:** Writing – review & editing. **Qiong Wu:** Writing – review & editing. **Rosella Pinna-Jamme:** Writing – review & editing, Investigation. **Andrew Tien-shun Lin:** Writing – review & editing, Resources.

Declaration of competing interest

The authors declare that they have no known competing financial interests or personal relationships that could have appeared to influence the work reported in this paper.

Acknowledgements

We thank the IFREMER (Institut Polaire Emile Victor), the crews and scientific teams of the HYDROSED research cruise for their excellent work during the pore fluids sampling. Y. Huang was supported by the China Postdoctoral Science Foundation (Grant No. 2024 M763692) and the National Natural Science Foundation of China (Grant No. 42506065). Q. Wu was supported by National Natural Science Foundation of China (Grant No. 42176058). We gratefully acknowledge the assistance provided by Louise Bordier during major and trace element analyses.

Appendix A. Supplementary data

Supplementary data to this article can be found online at https://doi.org/10.1016/j.chemgeo.2026.123355.

Data availability

I have shared data in the supplementary file

References

Abbott, A.N., 2019. A benthic flux from calcareous sediments results in non-conservative neodymium behavior during lateral transport: a study from the Tasman Sea. Geology 47, 363–366.
Abbott, A.N., Haley, B.A., McManus, J., Reimers, C.E., 2015. The sedimentary flux of dissolved rare earth elements to the ocean. Geochim. Cosmochim. Acta 154, 186–200.
Algeo, T.J., Lyons, T.W., 2006. Mo–total organic carbon covariation in modern anoxic marine environments: Implications for analysis of paleoredox and paleohydrographic conditions. Paleoceanogr 21, PA1016.
Alibo, D.S., Nozaki, Y., 1999. Rare earth elements in seawater: particle association, shale-normalization, and Ce oxidation. Geochim. Cosmochim. Acta 63, 363–372.
Anderson, R.F., 1982. Concentration, vertical flux, and remineralization of particulate uranium in seawater. Geochim. Cosmochim. Acta 46, 1293–1299.
Arndt, S., Jørgensen, B.B., LaRowe, D.E., Middelburg, J.J., Pancost, R.D., Regnier, P., 2013. Quantifying the degradation of organic matter in marine sediments: a review and synthesis. Earth Sci. Rev. 123, 53–86.
Bau, M., Dulski, P., 1996. Distribution of yttrium and rare-earth elements in the Penge and Kuruman iron-formations, Transvaal Supergroup, South Africa. Precambrian Res. 79, 37–55.
Bau, M., Dulski, P., 1999. Comparing yttrium and rare earths in hydrothermal fluids from the mid-atlantic ridge: implications for Y and REE behaviour during near vent mixing and for the Y/Ho ratio of proterozoic seawater. Chem. Geol. 155, 77–90.
Bau, M., Möller, P., Dulski, P., 1997. Yttrium and lanthanides in eastern Mediterranean seawater and their fractionation during redox-cycling. Mar. Chem. 56, 123–131.
Bayon, G., Lambert, T., Vigier, N., De Deckker, P., Freslon, N., Jang, K., Larkin, C.S., Piotrowski, A.M., Tachikawa, K., Thollon, M., Tipper, E.T., 2020. Rare earth element and neodymium isotope tracing of sedimentary rock weathering. Chem. Geol. 553, 119794.
Berner, R., 1980. Early Diagenesis: A Theoretical Approach. Princeton University Press.
Bertaz, J., Liu, Z., Colin, C., Dapoigny, A., Lin, A.T.-S., Li, Y., Jian, Z., 2024. Climatic and environmental impacts on the sedimentation of the SW Taiwan margin since the last deglaciation: geochemical and mineralogical investigations. Paleoceanogr. Paleoclimatol. 39, e2023PA004745.
Borowski, W.S., Paull, C.K., Ussler III, W., 1996. Marine pore-water sulfate profiles indicate in situ methane flux from underlying gas hydrate. Geology 24, 655–658.
Boudreau, B.P., 2000. The mathematics of early diagenesis: from worms to waves. Rev. Geophys. 38, 389–416.
von Breymann, M.T., Emeis, K.-C., Camerlenghi, A., 1990. Geochemistry of sediments from the Peru upwelling area: rusults from sites 680, 682, 685 and 6881. Geology 491–503.
Breymann, v., Brumsack, H.J., Emeis, K.C., 1992. Depositional and diagenetic behavior of barium in the Japan Sea. Proc. Ocean Drill. Program 651–665.
Calvert, S.E., Pedersen, T.F., 1993. Geochemistry of recent oxic and anoxic marine sediments: Implications for the geological record. Mar. Geol. 113, 67–88.
Chuang, P.-C., Yang, T.F., Wallmann, K., Matsumoto, R., Hua, C.Y., Chen, H., Lin, S., Sun, C.H., Li, H.C., Wang, Y., Dale, A.W., 2019. Carbon isotope exchange during anaerobic oxidation of methane (AOM) in sediments of the northeastern South China Sea. Geochim. Cosmochim. Acta 246, 138–155.
Costa, K.M., Nielsen, S.G., Wang, Y., Lu, W., Hines, S.K.V., Jacobel, A.W., Oppo, D.W., 2023. Marine sedimentary uranium to barium ratios as a potential quantitative proxy for Pleistocene bottom water oxygen concentrations. Geochim. Cosmochim. Acta 343, 1–16.
Dadson, S.J., Hovius, N., Chen, H., Dade, W.B., Hsieh, M.-L., Willett, S.D., Hu, J.-C., Horng, M.-J., Chen, M.-C., Stark, C.P., Lague, D., Lin, J.-C., 2003. Links between erosion, runoff variability and seismicity in the Taiwan orogen. Nature 426, 648–651.
Deng, K., Yang, S., Du, J., Lian, E., Vance, D., 2022. Dominance of benthic flux of REEs on continental shelves: implications for oceanic budgets. Geochem. Perspect. Lett. 22, 26–30.
Deng, Y., Ren, J., Guo, Q., Cao, J., Wang, H., Liu, C., 2017. Rare earth element geochemistry characteristics of seawater and porewater from deep sea in western Pacific. Sci. Rep. 7, 16539.
Du, J., Haley, B., Alan, C., Abbott, A., McManus, J., Vance, D., 2022. Reactive-transport modeling of neodymium and its radiogenic isotope in deep-sea sediments: the roles of authigenesis, marine silicate weathering and reverse weathering. Earth Planet. Sci. Lett. 596, 117792.
Du, J., Haley, B., McManus, J., Blaser, P., Rickli, J., Vance, D., 2025. Abyssal seafloor as a key driver of ocean trace-metal biogeochemical cycles. Nature 642, 620–627.

Elderfield, H., Sholkovitz, E.R., 1987. Rare earth elements in the pore waters of reducing nearshore sediments. Earth Planet. Sci. Lett. 82, 280–288.
Frimmel, H.E., 2009. Trace element distribution in Neoproterozoic carbonates as palaeoenvironmental indicator. Chem. Geol. 258, 338–353.
Froelich, P.N., Klinkhammer, G.P., Bender, M.L., Luedtke, N.A., Heath, G.R., Cullen, D., Dauphin, P., Hammond, D., Hartman, B., Maynard, V., 1979. Early oxidation of organic matter in pelagic sediments of the eastern equatorial Atlantic: suboxic diagenesis. Geochim. Cosmochim. Acta 43, 1075–1090.
Hage, S., Baker, M.L., Babonneau, N., Soulet, G., Dennielou, B., Silva Jacinto, R., Hilton, R.G., Galy, V., Baudin, F., Rabouille, C., Vic, C., Sahin, S., Açikalin, S., Talling, P.J., 2024. How is particulate organic carbon transported through the river-fed submarine Congo Canyon to the deep sea? Biogeoscience 21, 4251–4272.
Haley, B.A., Klinkhammer, G.P., McManus, J., 2004. Rare earth elements in pore waters of marine sediments. Geochim. Cosmochim. Acta 68, 1265–1279.
Haley, B.A., Wu, Y., Muratli, J., Basak, C., Pena, L., Goldstein, S., 2021. Rare earth element and neodymium isotopes of the eastern US GEOTRACES Equatorial Pacific Zonal Transect (GP16). Earth Planet. Sci. Lett. 576, 117223.
Hatje, V., Schijf, J., Johannesson, K.H., Andrade, R., Caetano, M., Brito, P., Haley, B.A., Lagarde, M., Jeandel, C., 2024. The global biogeochemical cycle of the rare earth elements. Glob. Biogeochem. Cycles 38, e2024GB008125.
Hesse, R., Schacht, U., 2011. Chapter 9 - early diagenesis of deep-sea sediments. In: Developments in Sedimentology, 63. Elsevier, pp. 557–713.
Hood, A., Noal, J., Malcolm, W., Wang, X., 2018. The effects of diagenesis on geochemical paleoredox proxies in sedimentary carbonates. Geochim. Cosmochim. Acta 232, 265–287.
Hu, C.-Y., Frank Yang, T., Burr, G.S., Chuang, P.-C., Chen, H.-W., Walia, M., Chen, N.-C., Huang, Y.-C., Lin, S., Wang, Y., Chung, S.-H., Huang, C.-D., Chen, C.-H., 2017. Biogeochemical cycles at the sulfate-methane transition zone (SMTZ) and geochemical characteristics of the pore fluids offshore southwestern Taiwan. J. Asian Earth Sci. 149, 172–183.
Hu, Z., Weynell, M., Su, N., Hohl, S., Han, Z., Wen, Y., Yang, S., 2025. Evidence from Mg isotopes indicating reverse weathering as a significant Mg sink in Tibetan Plateau lakes. Quarter. Sci. Rev. 349, 109138.
Huang, H., Liu, Z., Zhao, Y., Zhao, H., Fernandez, A.R., Colin, C., Lin, A.T.-S., 2023a. Clay mineral assemblages of late Holocene turbidites in the Gaoping Submarine Canyon of the northeastern South China Sea and their responses to typhoon activities. Palaeogeogr. Palaeoclimatol. Palaeoecol. 624, 111650.
Huang, Y., Colin, C., Liu, Z., Douville, E., Dapoigny, A., Haurine, F., Wu, Q., Tien-Shun Lin, A., 2023b. Impacts of nepheloid layers and mineralogical compositions of oceanic margin sediments on REE concentrations and Nd isotopic compositions of seawater. Geochim. Cosmochim. Acta 359, 57–70.
Huh, C.-A., Lin, H.-L., Lin, S., Huang, Y.-W., 2009. Modern accumulation rates and a budget of sediment off the Gaoping (Kaoping) river, SW Taiwan: a tidal and flood dominated depositional environment around a submarine canyon. J. Mar. Syst. 76, 405–416.
Huh, C.-A., Chen, W., Hsu, F.-H., Su, C.-C., Chiu, J.-K., Lin, S., Liu, C.-S., Huang, B.-J., 2011. Modern (<100 years) sedimentation in the Taiwan Strait: rates and source-to-sink pathways elucidated from radionuclides and particle size distribution. Cont. Shelf Res. 31, 47–63.
Kim, J.-H., Torres, M.E., Haley, B.A., Kastner, M., Pohlman, J.W., Riedel, M., Lee, Y.-J., 2012. The effect of diagenesis and fluid migration on rare earth element distribution in pore fluids of the northern Cascadia accretionary margin. Chem. Geol. 291, 152–165.
Kissel, C., Van Toer, A., Laj, C., Cortijo, E., Michel, E., 2013. Variations in the strength of the North Atlantic bottom water during Holocene. Earth Planet. Sci. Lett. 369-370, 248–259.
Li, Z.-X., Zhang, S.-B., Zheng, Y.-F., Wu, S.-T., Li, W.-C., Sun, F.-Y., Liang, T., 2022. Mobilization and fractionation of HFSE and REE by high fluorine fluid of magmatic origin during the alteration of amphibolite. Lithos 420-421, 106701.
Liu, J., Chen, Z., Yan, W., Chen, M., Yin, X., 2010. Geochemical Characteristics of rare Earth lements in the Fine-Grained Fraction of Surface Sediment from South China Sea. Earth Sci. J. China Univ. Geosci. 35, 563–571.
Liu, Z., Zhao, Y., Colin, C., Stattegger, K., Wiesner, M.G., Huh, C.-A., Zhang, Y., Li, X., Sompongchaiyakul, P., You, C.-F., Huang, C.-Y., Liu, J.T., Siringan, F.P., Le, K.P., Sathiamurthy, E., Hantoro, W.S., Liu, J., Tuo, S., Zhao, S., Zhou, S., He, Z., Wang, Y., Bunsomboonsakul, S., Li, Y., 2016. Source-to-sink transport processes of fluvial sediments in the South China Sea. Earth Sci. Rev. 153, 238–273.
Martín, J., Palanques, A., Vitorino, J., Oliveira, A., de Stigter, H.C., 2011. Near-bottom particulate matter dynamics in the Nazaré submarine canyon under calm and stormy conditions. Deep-Sea Res. II Top. Stud. Oceanogr. 58, 2388–2400.
McLennan, S.M., 2001. Relationships between the trace element composition of sedimentary rocks and upper continental crust. Geochem. Geophys. Geosyst. 2, 2000GC000109.
McManus, J., Berelson, W.M., Severmann, S., Poulson, R.L., Hammond, D.E., Klinkhammer, G.P., Holm, C., 2006. Molybdenum and uranium geochemistry in continental margin sediments: Paleoproxy potential. Geochim. Cosmochim. Acta 70, 4643–4662.
Moore, T.S., Murray, R.W., Kurtz, A.C., Schrag, D.P., 2004. Anaerobic methane oxidation and the formation of dolomite. Earth Planet. Sci. Lett. 229, 141–154.
Nozaki, Y., Zhang, J., Amakawa, H., 1997. The fractionation between Y and Ho in the marine environment. Earth Planet. Sci. Lett. 148, 329–340.
Owens, S.A., Buesseler, K.O., Sims, K.W.W., 2011. Re-evaluating the 238U-salinity relationship in seawater: implications for the 238U–234Th disequilibrium method. Mar. Chem. 127, 31–39.
Patton, G.M., Francois, R., Weis, D., Hathorne, E., Gutjahr, M., Frank, M., Gordon, K., 2021. An experimental investigation of the acquisition of Nd by authigenic phases of marine sediments. Geochim. Cosmochim. Acta 301, 1–29.
Paul, S.A.L., Haeckel, M., Bau, M., Bajracharya, R., Koschinsky, A., 2019a. Small-scale heterogeneity of trace metals including rare earth elements and yttrium in deep-sea sediments and porewaters of the Peru Basin, southeastern equatorial Pacific. Biogeoscience 16, 4829–4849.
Paul, S.A.L., Volz, J.B., Bau, M., Köster, M., Kasten, S., Koschinsky, A., 2019b. Calcium phosphate control of REY patterns of siliceous-ooze-rich deep-sea sediments from the central equatorial Pacific. Geochim. Cosmochim. Acta 251, 56–72.
Paytan, A., Griffith, E.M., 2007. Marine barite: recorder of variations in ocean export productivity. Deep-Sea Res. II Top. Stud. Oceanogr. 54, 687–705.
Schmitt, R.A., Smith, R.H., Lasch, J.E., Mosen, A.W., Olehy, D.A., Vasilevskis, J., 1963. Abundances of the fourteen rare-earth elements, scandium, and yttrium in meteoritic and terrestrial matter. Geochim. Cosmochim. Acta 27, 577–622.
Scholz, F., McManus, J., Mix, A., et al., 2014. The impact of ocean deoxygenation on iron release from continental margin sediments. Nature Geosci. 7, 433–437.
Sholkovitz, E.R., Piepgras, D.J., Jacobsen, S.B., 1989. The pore water chemistry of rare earth elements in Buzzards Bay sediments. Geochim. Cosmochim. Acta 53, 2847–2856.
Smrzka, D., Zwicker, J., Bach, W., Feng, D., Himmler, T., Chen, D., Peckmann, J., 2019. The behavior of trace elements in seawater, sedimentary pore water, and their incorporation into carbonate minerals: a review. Facies 65, 41.
Snyder, G.T., Hiruta, A., Matsumoto, R., Dickens, G.R., Tomaru, H., Takeuchi, R., Komatsubara, J., Ishida, Y., Yu, H., 2007. Pore water profiles and authigenic mineralization in shallow marine sediments above the methane-charged system on Umitaka Spur, Japan Sea. Deep-Sea Res. II Top. Stud. Oceanogr. 54, 1216–1239.
Steiner, Z., Antler, G., Berelson, W.M., Crockford, P.W., Dunlea, A.G., Hou, Y., Adkins, J. F., Turchyn, A.V., Achterberg, E.P., 2023. Trace element geochemistry in North Pacific red clay sediment porewaters and implications for water-column studies. Glob. Biogeochem. Cycles 37, e2023GB007844.
Torres, M.E., Teichert, B.M.A., Tréhu, A.M., Borowski, W., Tomaru, H., 2004. Relationship of pore water freshening to accretionary processes in the Cascadia margin: fluid sources and gas hydrate abundance. Geophys. Res. Lett. 31, L22305.
Wang, R., Williams, T.J., Hillenbrand, C.-D., Ehrmann, W., Larkin, C.S., Hutchings, A.M., Piotrowski, A.M., 2022. Boundary processes and neodymium cycling along the Pacific margin of West Antarctica. Geochim. Cosmochim. Acta 327, 1–20.
Wehrmann, L.M., Risgaard-Petersen, N., Schrum, H.N., Walsh, E.A., Huh, Y., Ikehara, M., Pierre, C., D'Hondt, S., Ferdelman, T.G., Ravelo, A.C., Takahashi, K., Zarikian, C.A., 2011. Coupled organic and inorganic carbon cycling in the deep subseafloor sediment of the northeastern Bering Sea Slope (IODP Exp. 323). Chem. Geol. 284, 251–261.
Williams-Jones, A.E., Migdisov, A.A., Samson, I.M., 2012. Hydrothermal Mobilisation of the rare earth elements - a Tale of "Ceria" and "Yttria". Elements 8, 355–360.
Wu, Q., Colin, C., Liu, Z., Douville, E., Dubois-Dauphin, Q., Frank, N., 2015. New insights into hydrological exchange between the South China Sea and the Western Pacific Ocean based on the Nd isotopic composition of seawater. Deep-Sea Res. II Top. Stud. Oceanogr. 122, 25–40.
Yano, M., Yasukawa, K., Nakamura, K., Ikehara, M., Kato, Y., 2020. Geochemical features of redox-sensitive trace metals in sediments under oxygen-depleted marine environments. Minerals 10, 1021.
Yu, S.-W., Tsai, L.L., Talling, P.J., Lin, A.T., Mii, H.-S., Chung, S.-H., Horng, C.-S., 2017a. Sea level and climatic controls on turbidite occurrence for the past 26kyr on the flank of the Gaoping Canyon off SW Taiwan. Mar. Geol. 392, 140–150.
Yu, Z., Colin, C., Douville, E., Meynadier, L., Duchamp, S., Sepulcre, S., Wan, S., Song, L., Wu, Q., Xu, Z., Bassinot, F., 2017b. Yttrium and rare earth element partitioning in seawaters from the Bay of Bengal. Geochem. Geophys. Geosyst. 4, 1388–1403.
Zhang, X., Liu, Z., Li, D., Zhao, Y., Zhang, Y., 2024. Turbidity currents regulate the transport and settling of microplastics in a deep-sea submarine canyon. Geology 52, 646–650.
Zhang, Y., Liu, Z., Zhao, Y., Colin, C., Zhang, X., Wang, M., Zhao, S., Kneller, B., 2018. Long-term in situ observations on typhoon-triggered turbidity currents in the deep sea. Geology 46, 675–678.
Zwicker, J., Smrzka, D., Himmler, T., Monien, P., Gier, S., Goedert, J.L., Peckmann, J., 2018. Rare earth elements as tracers for microbial activity and early diagenesis: a new perspective from carbonate cements of ancient methane-seep deposits. Chem. Geol. 501, 77–85.